Microporous and Mesoporous Materials 276 (2019) 260–269

Contents lists available at ScienceDirect

Microporous and Mesoporous Materials

journal homepage: www.elsevier.com/locate/micromeso

Mesopore differences between pillared lamellar MFI and MWW zeolites probed by atomic layer deposition of titania and consequences on photocatalysis

Junyan Zhang[a], Zheng Lu[b], Wei Wu[a], Dat T. Tran[c], Wenjin Shang[d], Huiyong Chen[d], Yu Lei[b], Zhenglong Li[e], Mei Wang[a], Taylor J. Woehl[a], Dongxia Liu[a,*]

[a] Department of Chemical and Biomolecular Engineering, University of Maryland, College Park, MD, 20742, USA
[b] Department of Chemical and Materials Engineering, University of Alabama in Huntsville, Huntsville, AL, 35899, USA
[c] U. S. Army Research Laboratory, RDRL-SED-E, 2800 Powder Mill Road, Adelphi, MD, 20783, USA
[d] School of Chemical Engineering, Northwest University, Xi'an, Shanxi, 710069, China
[e] Energy & Transportation Sciences Division, Oak Ridge National Laboratory, Oak Ridge, TN, 37831, USA

ARTICLE INFO

Keywords:
Pillared zeolite
Lamellar zeolite
Atomic layer deposition
Mesoporosity
Photocatalysis

ABSTRACT

The pillared MWW (PMWW or MCM-36) and pillared MFI (PMFI) are two prominent representatives of meso-/microporous lamellar zeolites, which are made by pillaring of layered MCM-22(P) and multilamellar MFI precursors, respectively. They both consist of a 10-membered ring sinusoidal micropore channel within each zeolitic layer and mesopore voids created by pillars between two adjacent zeolitic layers. Although catalytic activities of PMWW and PMFI have been compared, identification of mesopore differences between these two pillared lamellar zeolites has not been attempted. In this work, we report the differences in mesopore characteristics between PMWW and PMFI zeolites probed by atomic layer deposition (ALD) of titania (ALD-TiO_2) species and a combination of structural, textural, composition and catalytic property analyses of the samples before and after ALD treatment, respectively. The results suggest PMFI has cylindrical mesopores with uniform sizes from pore entrance to main body, while PMWW has ink-bottle mesopores with the neck size much smaller than pore body. The communication between micropore and mesopore in PMFI is direct, but no communication exists in PMWW zeolites. The ALD-TiO_2 process considerably modified external surface composition of PMFI and PMWW zeolites, which consequently led to a new application of the pillared lamellar zeolite materials, i.e., photo-catalytically active meso-/microporous zeolites for environmental remedy reactions.

1. Introduction

Layered (or called two-dimensional (2D)) zeolite materials generally contain a stack of microporous crystalline aluminosilicate sheets, each of which has one or a fraction of the unit-cell thickness, equivalent to a few nanometers [1–4]. The atoms within the zeolitic layers are connected by strong covalent bonds while the contiguous zeolitic layers are linked by weak van der Waals force or hydrogen bonds. The weak interlayer interactions in 2D zeolites determine a variety of structural and chemical modifications that can be potentially made in the gallery of adjacent zeolitic layers, with preservation of the original layer integrity. Therefore, 2D zeolite materials can be recognized as host scaffolds that can expand and/or extend via structural, topotactic and compositional modifications to form novel and diverse hierarchical structures.

Two basic chemical processes, exfoliation [5–10] and pillarization [11–16], have been used to modify 2D zeolites into diverse zeolitic structures. The exfoliation process separates the stack of 2D zeolite nanosheets into self-standing independent entities by breaking down the weak interlayer interactions. The exfoliated zeolite nanosheets can be basis materials for fabrication of zeolite membranes [8,17,18] and used directly as hierarchical catalysts [5,19] with high surface area and active site accessibility for reactions. In comparison to breaking down the stack of 2D zeolites in the exfoliation process, the pillarization process transforms the 2D zeolites into a hierarchical micro- and mesoporous materials with the retention of the stacked layer structure. The pillarization often involves subsequent expansion of interlayer space by swelling with long chain polar organic molecules, intercalation of the swollen materials with liquid inorganic oxide precursors, hydrolysis of entrapped inorganic oxide precursors, and removal of organics as well

* Corresponding author.
E-mail address: liud@umd.edu (D. Liu).

https://doi.org/10.1016/j.micromeso.2018.10.009
Received 4 June 2018; Received in revised form 30 September 2018; Accepted 12 October 2018
Available online 13 October 2018
1387-1811/

as transformation of inorganic oxide precursors into permanent oxide pillars between zeolitic layers by calcination [11–15]. The replacement of inorganic oxide precursors with organic compounds and the calcination step with acid extraction can produce organic pillared 2D zeolites [16,20,21]. Pillared lamellar zeolites with hierarchical structures and compositions have been created for adsorption and catalysis applications [22–25].

As prominent representatives of layered 2D zeolite precursors, MCM-22(P) [11] and multilamellar MFI [26] have been widely studied in the pillarization processes. For example, MCM-22(P) was pillared by tetraethyl orthosilicate (TEOS, the precursor of silica), reported by Mobil scientists in 1990s [12,27] to form the first synthesized pillared 2D zeolite, pillared MWW (PMWW or MCM-36). Multilamellar MFI was pillared by silica to form pillared MFI (PMFI) by Ryoo's group in recent year [14]. PMFI and PMWW have quite similar topological features given the fact that they both consist of a 10-membered ring (10 MR) sinusoidal micropore channel within each zeolitic layer and mesopore voids created by pillars between two adjacent zeolitic layers. The presence of mesopores results in high surface area and acid site accessibility to bulky molecules in PMFI and PMWW zeolites [23,24,28]. Although the textural and catalytic properties of PMWW and PMFI zeolites have been understood, identification for differences of mesopore structures and further modification of these materials for diverse applications have rarely been studied.

In this work, we report the exploration on mesopore structure differences between PMFI and PMWW zeolites. Atomic layer deposition (ALD) of titania (TiO_2) has been used as a tool to probe the interactions between the incoming TiO_2 precursor and the mesopores in both zeolites. ALD process involves alternating and self-limiting reactions between gaseous precursors and the solid mesopore surface, which realizes the precise deposition of materials in an atomic layer-by-layer fashion [29–31]. This offers a unique opportunity to exploit the fine structural characteristics of mesopores in pillared lamellar zeolites. A combinational analysis on the textural and compositional properties of PMFI and PMWW zeolites before and after ALD treatment has been conducted to understand their mesopore differences. As a semiconductor material, titania is photo-responsive catalyst for photocatalytic reactions. The introduction of titania onto 2D zeolites by ALD enables photocatalytic 2D zeolite materials for photocatalysis applications. The performance of titania modified PMFI and PMWW zeolites in photocatalytic reactions was studied and further correlated to their mesopore structure differences.

2. Experimental

2.1. Preparation of PMFI and PMWW zeolites

The PMFI zeolite was synthesized from the multilamellar MFI precursor, which was prepared following the recipe reported by Choi et al. [26] Pillaring of multilamellar MFI to obtain PMFI was carried out by using procedure reported by Na et al. [14] The PMWW was synthesized following the method reported by Maheshwari et al. [32] by pillaring the precursor MCM-22(P) with TEOS. An ion-exchange procedure was also applied to PMFI and PMWW to make for proton-form zeolite prior to the ALD modification processes. Details on the synthesis of PMFI and PMWW zeolites are described in section S1 of the Supporting Information.

2.2. ALD-TiO_2 modification of PMFI and PMWW zeolites

ALD-TiO_2 modification of PMWW and PMFI zeolites was performed in a viscous flow benchtop reactor (Gemstar-6, Arradiance), as the one used in our previous study [33]. A typical deposition of TiO_2 on high surface area substrates using ALD has been discussed in detail elsewhere [34]. In short, 0.15 g of PMFI or PMWW sample was uniformly spread onto a stainless steel tray covered by a mesh. The TiO_2 was deposited at temperatures of 473 K. The alternating exposure time of titanium isoperoxide (TTIP) and deionized (DI) water was 25 s and 3.75 s, respectively. A 200s purge time was used in between precursor exposure. One and five ALD cycles of TiO_2, respectively, were used for modification of PMFI and PMWW zeolites. The resultant zeolite samples were designated as PMFI-ALD-1, PMFI-ALD-5, PMWW-ALD-1 and PMWW-ALD-5, in which the digits stand for the number of ALD cycles.

2.3. Catalyst characterization

Powder X-Ray diffraction (XRD) patterns were recorded using a Bruker D8 Advance Lynx Powder Diffractometer (LynxEye PSD detector, sealed tube, Cu Kα radiation with Ni β-filter). Scanning electron microscopy (SEM) images were recorded on a Quanta 200F scanning electron microscope. The location of TiO_2 species was observed using high-angle annular dark-field scanning transmission electron microscopy (HAADF-STEM, JEOL JEM-2100 FEG). The nitrogen (N_2) and argon (Ar) isotherms were measured at 77 K and 87 K, respectively, in an Autosorb-iQ analyzer (Quantachrome Instruments). Before measurement, the zeolite samples were degassed overnight at 623 K and 1 mm Hg pressure. Si, Ti, and Al contents of the zeolite samples were determined by inductively coupled plasma optical emission spectroscopy (ICP-OES, Perkin Elmer Optima 7000). The surface Si, Al and Ti concentrations were quantified using a X-ray photon spectrometer (Kratos AXIS 165) equipped with 165 mm radius hemispherical analyzer and eight channeltron detection system coupled with monochromatic Al radiation (1486.6 eV). Diffuse reflectance (DR) Ultraviolet–Visible (UV–Vis) spectra were obtained using an Ocean Optics USB2000 + spectrometer equipped with an IS200-4 integrating sphere detector, and the white high reflectance sphere material (manufactured from Polytetrafluoroethylene (PTFE) based bulk material) was used as the reference.

2.4. Photocatalytic reactions over ALD-TiO_2 modified PMFI and PMWW zeolites

To test the photocatalytic performance of ALD-Ti modified PMFI and PMWW zeolites, the liquid phase catalytic degradation of methyl orange (MO) molecules under light irradiation was employed. A 200 W HBO Mercury (Hg) lamp (OSRAM, Germany) was chosen as the light source, which was located 15 cm away from the reactor. Liquid samples were withdrawn at 1 h intervals and MO decomposition was analyzed by a Lambda 40 UV/Vis spectrophotometer (PerkinElmer Instruments). To further evaluate the photocatalytic performance of ALD-Ti modified PMFI and PMWW zeolites, the CO_2 reduction reaction was performed in a cylindrical batch reactor under ambient conditions. A Xenon lamp (450 W) was used as the light source to shine the reactor through a quartz window. After 4 h of irradiation, the Xe lamp was turned off and the gas mixture in the reactor was analyzed by a gas-chromatography (Agilent Technologies, 6890 N) through an automated gas valve. Section S1.3 of the supporting information includes the details of procedure for testing photocatalytic activity of PMFI and PMWW after TiO_2 ALD.

3. Results and discussion

3.1. Morphology and structure of TiO_2 ALD modified PMFI and PMWW zeolites

To examine the influences of TiO_2 ALD treatment on the morphology and crystalline structure of PMFI and PMWW zeolites, SEM and XRD measurements were conducted on the samples before and after the ALD process, respectively. Fig. S1 in supporting information shows SEM images of bare PMFI and PMWW zeolites and after 1 and 5 ALD cycles of TiO_2 treatments. As indicated in Figs. S1(A)–(C), PMFI, PMFI-ALD-1 and PMFI-ALD-5 zeolites share the similar morphology, all of which

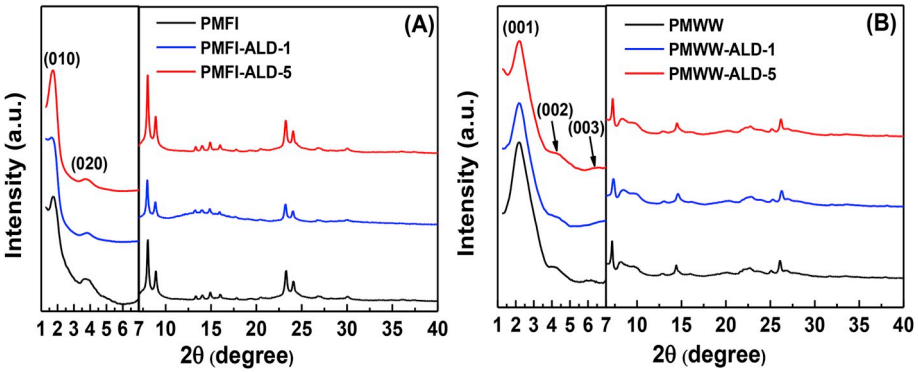

Fig. 1. Low- and high-angle XRD patterns of PMFI, PMFI-ALD-1, and PMFI-ALD-5 (A) and PMWW, PMWW-ALD-1, and PMWW-ALD-5 (B), respectively.

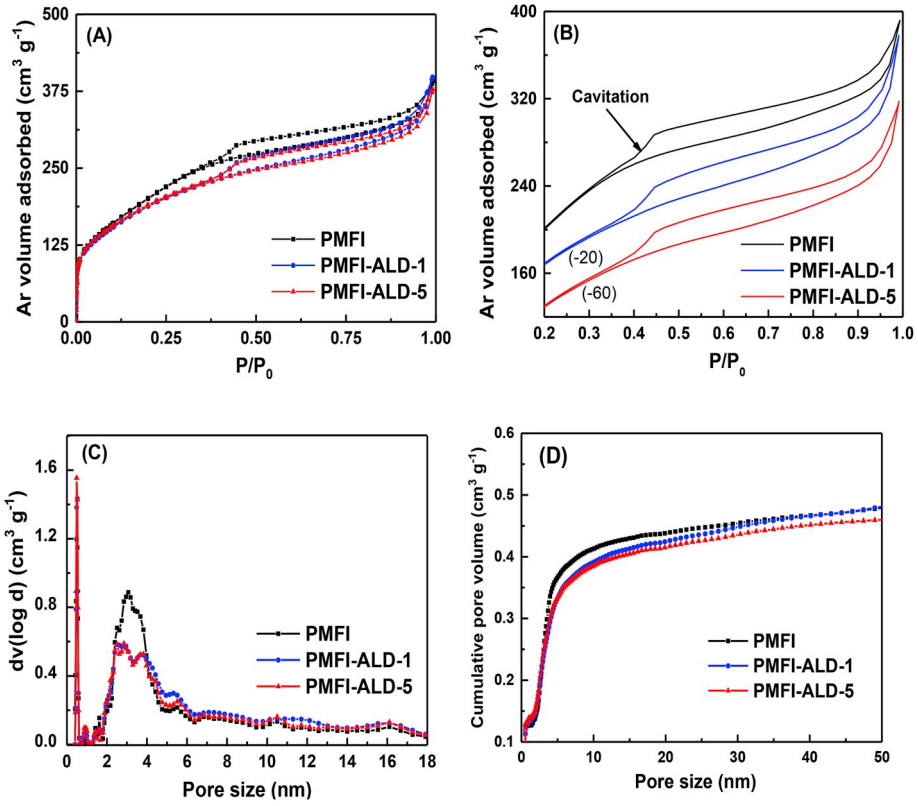

Fig. 2. Ar adsorption-desorption isotherms (A), hysteresis loops in isotherms (B), NLDFT pore size distribution (C), and cumulative pore volume versus pore size (D), of PMFI, PMFI-ALD-1, and PMFI-ALD-5, respectively.

have zeolite layers aggregated into flower-like structure. PMWW, PMWW-ALD-1 and PMWW-ALD-5 in Figs. S1(D)–(F) in sequence have nanolayers stacked into flake-like structure. Overall, the TiO_2 ALD process didn't cause obvious morphology change in either PMFI or PMWW zeolite.

Fig. 1 shows low- and high-angle XRD data of PMFI, PMFI-ALD-1, PMFI-ALD-5, PMWW, PMWW-ALD-1 and PMWW-ALD-5 samples. In Fig. 1(A), three PMFI-based samples have nearly the same characteristic diffraction pattern of MFI zeolite in the diffraction angle range of 7–40°. This indicates that ALD of TiO_2 did not change crystalline structure of zeolitic layers in PMFI. The absence of any diffraction peak relevant to titania materials in Fig. 1(A) is ascribed to its low-loading amount (< 1 wt%, Table 2) in the resultant zeolite samples. PMFI, PMFI-ALD-1 and PMFI-ALD-5 also have similar XRD peak positions, corresponding to the first-order (010) and second-order (020) of reflections from layered structure, in the low-angle range (2θ = 1-7°). This suggests that TiO_2 ALD process did not destroy, collapse or expand the zeolitic layers in the PMFI zeolite. The presence of the second-order reflection in all the PMFI-based zeolites indicates that the long-range structural order is retained in the TiO_2 ALD process. In particular, the (010) peak around 2θ ~1.70° in Fig. 1(A) corresponds to a spacing distance of ~5.19 nm. The average interlayer distance between two zeolitic layers in PMFI is calculated by subtracting the thickness of the layer (along with b-axis direction of MFI, ~3.40 nm [7]) from interlayer spacing distance, which is around 1.79 nm.

The low- and high-angle XRD patterns of PMWW, PMWW-ALD-1 and PMWW-ALD-5 samples are shown in Fig. 1(B). For the high-angle XRD data (2θ = 7–40°), three samples have nearly same XRD peak positions, closely resembled the patterns reported by Roth et al. [35], indicating the preservation of the crystal structure within the zeolitic layer in the TiO_2 ALD process. Similarly, no peaks corresponding to titania phases are observed due to the deposition of titania species is too small (< 1 wt%, Table 2) to be pronouncedly detected in PMWW zeolite. The low-angle XRD data (2θ = 1–7°) kept the same diffraction

peaks that are attributed to the first-, second- and third-order of reflections in sequence in the PMWW, PMWW-ALD-1 and PMWW-ALD-5 samples, suggesting the preservation of the long range of ordered layered structure in PMWW through the TiO_2 ALD process. The average interlayer distance between two zeolitic layers in PMWW is calculated in a similar way to that of PMFI. By subtracting the thickness of the layer (along with c-axis direction of MWW, ~2.60 nm [7]) from interlayer spacing distance, which is around 4.01 nm, the average interlayer distance is around 1.41 nm, slightly smaller than that of PMFI zeolite.

3.2. Textural properties of TiO_2 ALD modified pillared lamellar zeolites

3.2.1. TiO_2 ALD modified PMFI zeolites

To understand the textural properties of PMFI and PMWW zeolites before and after TiO_2 ALD, we carried out Ar adsorption-desorption measurements on these samples. Fig. 2 shows the Ar adsorption-desorption isotherms, nonlocal density functional theory (NLDFT) pore size distributions calculated from the adsorption branch of Ar isotherms using a cylinder pore model, and cumulative pore volume versus pore size for PMFI, PMFI-ALD-1 and PMFI-ALD-5 samples. As shown in Fig. 2(A), PMFI, PMFI-ALD-1 and PMFI-ALD-5 have nearly same Ar uptake at relative pressures of $P/P_0 < 0.10$, which indicates all of them have similar microporosity. The increase of adsorption volume with increasing relative pressures at $P/P_0 > 0.10$ is caused by mesopores in these materials. Apparently, PMFI has higher Ar uptake compared to PMFI-ALD-1 and PMFI-ALD-5 in this relative pressure range, suggesting higher mesoporosity in PMFI before TiO_2 ALD treatment. A comparison on Ar uptake between PMFI-ALD-1 and PMFI-ALD-5 indicates that the former has slightly higher adsorption at $P/P_0 > 0.55$, which is equivalent to its higher meso- and/or macroporostiy. Hysteresis loops, due to capillary condensation of adsorptive atoms/molecules in mesopores, are observed [36]. Fig. 2(B) shows the Ar isotherms that are purposely separated one from another for the clarity of hysteresis loops, all of which have H4 type, consistent with complex micro-/mesopore network in hierarchical zeolite [3]. The width of the hysteresis loop, in Fig. 2(B), gently decreases from PMFI, to PMFI-ALD-1 and then to PMFI-ALD-5 sample, which indicates the decrease in mesopore sizes due to TiO_2 ALD. The lower limits (or closures) of the of the hysteresis loops are similar, reflecting they have similar cavitation pressures [37,38]. The Ar isotherms hint that TiO_2 ALD did not reduce microporosity of PMFI but decreased its mesoporostiy. This is consistent with inaccessibility of metal oxide precursors to zeolite micropores due to the subtle differences in diameters of precursor molecules and zeolite pore apertures [39–42] and accessibility of precursor molecules to mesopores due to the larger mesopore size compared to molecule diameters [33,42,43]. One ALD cycle of TiO_2 preferentially led to decrease in mesoporosity, while five ALD cycles of TiO_2 contributed to the decrease in the macroporosity that may forms from the interparticular voids. Table 1 summarizes the micropore volume and surface area, Brunauer–Emmett–Teller (BET) surface area and total pore volume, and external surface area and mesopore volume of PMFI before and after TiO_2 ALD.

The NLDFT pore size distributions of PMFI, PMFI-ALD-1 and PMFI-ALD-5 samples in Fig. 2(C) show that the micropore size is centred at ~0.51 nm, consistent with 10-MR micropore channels within zeolitic layers, and the mesopore size spans from 1.8 to 6.5 nm with a peak of ~3.0 nm, implying a broader mesopore size distribution. The TiO_2 ALD led to decrease in mesoporosity, reflected by the decrease in peak intensity in PMFI-ALD-1 and PMFI-ALD-5 samples in Fig. 2(C). It should be noted that the center of mesopore distribution in Fig. 2(C) is different from the interlayer spacing distance that is calculated from low-angle XRD data in Fig. 1(A). It can be speculated that the mesopores might be cylinder-like shape running in parallel with, instead of normal to, zeolitic layers in PMFI structure, similar to that reported for PMWW structure before [44]. Fig. 2(D) shows the cumulative pore volume versus pore sizes of these three zeolites. Clearly, the mesopore volume decreased obviously after one cycle of ALD-TiO_2 treatment, while large pores (> ~20 nm) reduced prominently after five cycles of treatment.

Table 1
Textural properties of PMFI and PMWW zeolites derived from Ar isotherms before and after ALD-TiO_2 process, respectively.

Zeolite	V_{micro} [a] ($cm^3\ g^{-1}$)	S_{micro} [a] ($m^2\ g^{-1}$)	S_{BET} [b] ($m^2\ g^{-1}$)	S_{ext} [c] ($m^2\ g^{-1}$)	V_t [d] ($cm^3\ g^{-1}$)	V_{mes} [e] ($cm^3\ g^{-1}$)
PMFI	0.117	304	678	374	0.429	0.312
PMFI-ALD-1	0.110	291	617	325	0.416	0.306
PMFI-ALD-5	0.114	296	616	320	0.404	0.290
PMWW	0.111	271	664	393	0.521	0.410
PMWW-ALD-1	0.101	273	626	353	0.460	0.359
PMWW-ALD-5	0.100	279	621	342	0.444	0.344

[a] Determined from t-plot method.
[b] Determined from Brunauer, Emmett, and Teller (BET) method.
[c] Calculated by $S_{ext} = S_{BET} - S_{micro}$.
[d] Calculated by N_2 adsorption at $P/P_0 = 0.95$.
[e] Determined from $V_{meso} = V_t - V_{micro}$.

Table 2
Composition of PMFI and PMWW zeolites determined from elemental analysis before and after ALD-TiO_2 process, respectively.

Zeolite	Si/Al ratio[a]	Si/Ti ratio[a]	Si/Ti ratio[b]	TiO_2 (wt %)[c]
PMFI	67	–	–	0.00
PMFI-ALD-1	75	559	33	0.23
PMFI-ALD-5	74	162	10	0.80
PMWW	30	–	–	0.00
PMWW-ALD-1	29	210	18	0.61
PMWW-ALD-5	29	144	10	0.88

[a] Determined by ICP-OES analysis.
[b] Determined by XPS analysis.
[c] Calculated from ICP-OES data.

The pore size distribution analyzed from the adsorption branch of Ar isotherms corresponds to the sizes of pore bodies due to a progressive filling of these pores [45,46]. To understand the structure feature of pore entrances (or necks), we derived the pore size distributions from the desorption branches of Ar isotherms by applying the NLDFT equilibrium transition kernel on the basis of a cylindrical pore model. The isotherms and pore size distributions were also analyzed by using a different adsorptive (N_2) on the PMFI, PMFI-ALD-1 and PMFI-ALD-5 zeolites to identify the artifact, i.e., cavitation, in the pore size distribution data for pore entrances. Fig. 3(A) compares the N_2 and Ar isotherms for these three zeolites. The pore size distributions derived from desorption branches of isotherms are collectively shown in Fig. 3(B). For easy comparison and clarity, the isotherms (Fig. S2(A)-(C)) and pore size distribution plots (Fig. S2(D)-(F) are represented in pairwise and compared to that calculated from the adsorption branch (Fig. S2(G)-(I)). In Fig. 3(A), the closed points of the hysteresis loops between N_2 and Ar isotherms in each of the PMFI, PMFI-ALD-1 and PMFI-ALD-5 samples are markedly different, suggesting the occurrence of cavitation phenomenon [45,47]. The cavitation during adsorbate desorption was confirmed by non-identical pore size distributions derived from desorption branches of Ar and N_2 isotherms (Fig. 3(B)) and differences in pore size distributions evaluated from the adsorption and desorption of Ar isotherms (Fig. S2(G)-(I)). The step-down characteristic in the desorption branch of the hysteresis loops in isotherms is not associated with the evaporation of condensed liquid from a specific group of pores, but is caused by the spontaneous evaporation of metastable pore liquid (cavitation, i.e., the tensile strength effect). This is equivalent to the artifact peak in the desorption pore size distribution curve [45,48]. Except for this artifact peak, the micropore and mesopore sizes evaluated from each method agree well. The decrease in

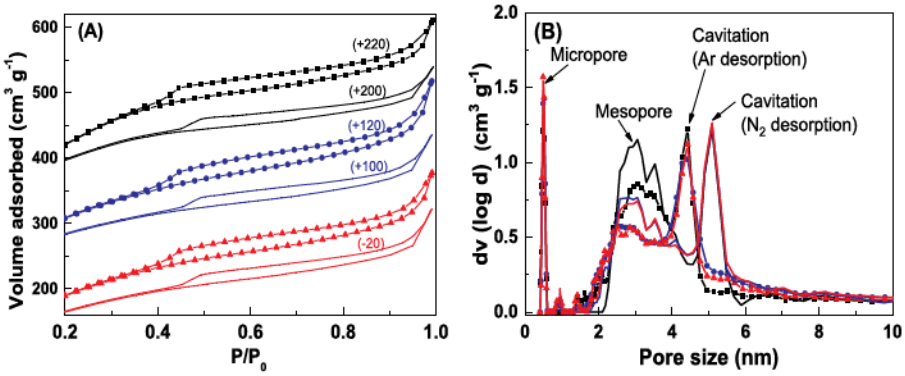

Fig. 3. N_2 (line) and Ar (line + symbol) adsorption–desorption isotherms (A) and NLDFT pore size distributions derived from the desorption branches of isotherms (B) of the PMFI (coded with black color), PMFI-ALD-1 (coded with blue color) and PMFI-ALD-5 (coded with red color) zeolites. (For interpretation of the references to color in this figure legend, the reader is referred to the Web version of this article.)

mesopore peak centred at ~3 nm with TiO_2 ALD cycles in PMFI (Fig. 3(B)) suggests that the pore entrance size decreases in similar degree to that of pore bodies.

3.2.2. TiO_2 ALD modified PMWW zeolites

We carried out the same textural property measurements on the PMWW, PMWW-ALD-1 and PMWW-ALD-5 as those done on PMFI-based zeolites. Fig. 4(A) shows the Ar adsorption-desorption isotherms. The similar Ar adsorption at $P/P_0 < 0.1$ indicates that all three PMWW-based samples have similar microporosity [49], which is not influenced by the ALD process due to inaccessibility of TTIP molecules to 10-MR mciropore channel. The increase in the adsorption volume up to relative pressures of $P/P_0 \sim 0.95$ indicates capillary condensation in the mesopores. The decrease in adsorption in the relative pressure range of $P/P_0 = 0.25$–0.95 from PMWW to PMWW-ALD-1 and then to PMWW-ALD-5 shows that decrease in mesoporosity with execution of ALD-TiO_2 cycles. Apparently, the first cycle of ALD-TiO_2, in comparison to the fifth cycles, led to significant decrease in mesoporosity in PMWW zeolite. This is also reflected by the textural parameters of surface areas and pore volumes summarized in Table 1. Different from ALD-TiO_2 of PMFI zeolite, five cycles of this process did not contribute obviously to the decrease in macroporosity including those from the interparticular voids. This can be correlated to the morphology differences between PMFI and PMWW: the former has layered particles aggregated into flower-like structure that could led to multiple levels of macroporosity, while the later has dispersed flake-like particles that do not produce same degrees of macoporosity among zeolite particles. The hysteresis loops in H4 type were purposely plotted in Fig. 4(B) to zoom in their fine features. The width of the hysteresis loop obviously decreases from PMWW, to PMWW-ALD-1 and then to PMWW-ALD-5, which indicates the distinct decrease in Ar uptake in mesopores due to TiO_2 deposition. The closing point of the hysteresis loops moves to higher P/P_0 with ALD process, reflecting less severe cavitation in PMWW-ALD-5 and PMWW-ALD-1 compared to PMWW zeolite [37,38].

The NLDFT pore size distributions of PMWW, PMWW-ALD-1 and PMWW-ALD-5 are plotted in Fig. 4(C). The micropore size distribution centers ~0.52 nm, consistent with 10 MR of MCM-22 zeolite [11,50]. The mesopore sizes spanning a range of 2–6 nm are similar to those of PMFI-based zeolites. However, the mesopores with a size range of 6–16 nm weigh obviously in Fig. 4(C) compared to the same mesopore

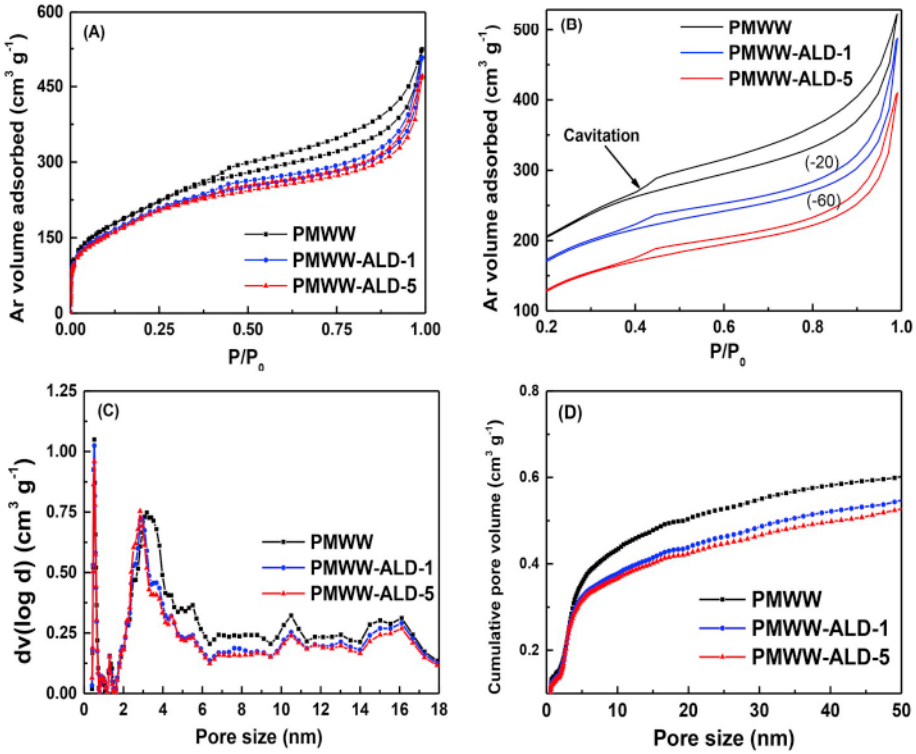

Fig. 4. Ar adsorption-desorption isotherms (A), hysteresis loops in isotherms (B), NLDFT pore size distribution (C), and cumulative pore volume versus pore size (D), of PMWW, PMWW-ALD-1, and PMWW-ALD-5, respectively.

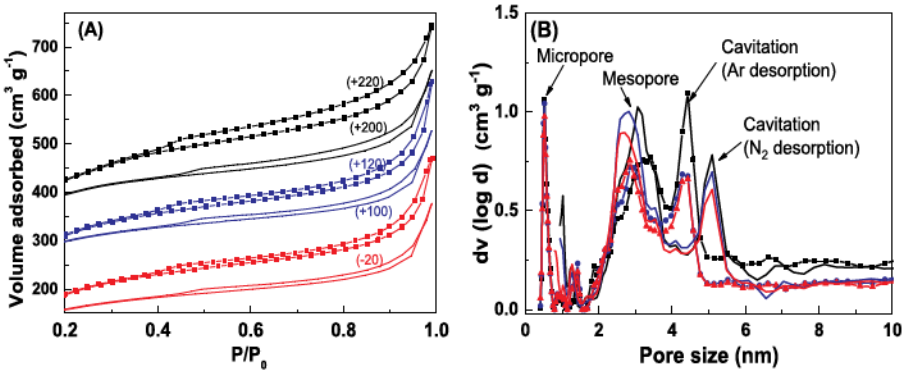

Fig. 5. N_2 (line) and Ar (line + symbol) adsorption–desorption isotherms (A) and NLDFT pore size distributions derived from the desorption branches of isotherms (B) of the PMWW (coded with black color), PMWW-ALD-1 (coded with blue color) and PMWW-ALD-5 (coded with red color) zeolites. (For interpretation of the references to color in this figure legend, the reader is referred to the Web version of this article.)

size range in Fig. 2(C), which suggests that PMWW has more diverse mesopore sizes compared to PMFI zeolites. The application of ALD-TiO_2 process led to mesoporosity decrease in PMWW, reflected by peak intensity drop with pore size > 3 nm, but the peak intensity did not change when the pore size is < 3 nm. This hints a fraction of mesopore in PMWW was not influenced by the ALD-TiO_2 process. Also, the measured mesopore sizes of PMWW-based zeolites from Ar isotherms are different from the interlayer spacing distance calculated from low-angle XRD data in Fig. 1(B), which means that cylinder-like mesopores should preferentially run in parallel with zeolitic layers. The cumulative pore volume versus pore sizes in Fig. 4(D) shows that the micropore size did not change with the number of ALD cycles, while both mesopore and marcorpore were decreased concurrently in the ALD-TiO_2 one cycle and five cycles. It should be noted that the 5 cycles of ALD processes did not cause very different pore volume loss compared to one cycle in PMWW zeolite. This might suggest that one cycle of ALD-TiO_2 has blocked entrance of TTIP into mesopores in later ALD cycles in PMWW zeolite.

We also analyzed the pore entrance properties in PMWW, PMWW-ALD-1 and PMWW-ALD-5 zeolites. The Ar and N_2 isotherms and pore size distributions derived from the desorption branches of both isotherms for these three zeolites are collectively shown in Fig. 5(A) and (B), respectively. Figs. S3(A)–(C) and (D)-(F) represent the isotherm and pore size distribution data plotted in pairwise and comparison of pore size distribution to that calculated from the adsorption branch (Fig. S3(G)-(I)). The pore size distributions of each material analyzed from different methods agree well except for the artifact peak due to cavitation in the desorption process. The small peak around 1 nm might be due to a phase transition in the N_2 adsorbate, which has been previously reported for certain MFI zeolite samples [51,52]. With increasing ALD-TiO_2 cycles, the artifact peak decreases significantly, while the mesopore entrances with sizes below ~3 nm keeps nearly constant (Fig. 5(B)). This reflects different mesopore characteristics in PMWW compared to PMFI although both pillared lamellar zeolites have very similar structure.

3.3. Composition of TiO_2 ALD modified PMFI and PMWW zeolites

The bulk compositions of PMWW and PMFI zeolites before and after TiO_2 ALD were measured by ICP-AES, and the results are shown in Table 2. For both PMWW and PMFI zeolites, the TiO_2 ALD did not cause obvious changes in Si/Al ratios, while Si/Ti ratio was decreased with ALD cycles due to inclusion of TiO_2 into the materials. We calculated the TiO_2 content in PMFI-ALD-1, PMFI-ALD-5, PMWW-ALD-1 and PMWW-ALD-5 from ICP-AES data, which showed 0.23 wt%, 0.80 wt%, 0.61 wt% and 0.88 wt% TiO_2 in sequence. The first ALD cycle of TiO_2 introduced nearly 3 times higher TiO_2 into PMWW compared to PMFI, while they both have similar TiO_2 content after fifth ALD cycle of TiO_2. The surface Ti composition of these materials was examined by XPS analyses. The Si/Ti ratio in zeolite surface is much lower than that of the bulk zeolite. This suggests that TiO_2 from ALD process was predominantly deposited onto zeolite external surface and mesopores, which is consistent with inaccessibility of TTIP to 10-MR micropores of PMFI and PMWW zeolites.

3.4. Comparison of mesopore characteristics between PMFI and PMWW zeolites

To understand the mesopore differences between PMFI and PMWW zeolites, we linked the mesopore volume loss to weight gain from TiO_2 deposition, and both of them to the number of ALD cycles, to draw the picture of mesopore characteristics in PMFI and PMWW zeolites. Table 3 shows that both the mesopore volume loss and TiO_2 content gain are increased with the number of ALD cycles in either PMFI or PMWW, but PMWW has much higher degree of mesopore volume loss compared to PMFI. In particular, both mesopore volume loss and TiO_2 content gain are distinctly higher in PMWW than PMFI after the first ALD cycle. The mesopore volume loss per ALD cycle (the fifth entry in Table 3) is similar after the first and fifth ALD cycles in PMFI, but significantly different in PMWW. The same trend is observed for the TiO_2 gain per ALD cycle, shown in the sixth entry in Table 3. The ratio

Table 3
Correlations among number of ALD cycle, mesopore volume loss, and weight gain from TiO_2 deposition in PMFI and PMWW zeolites.

Zeolite	Number of ALD cycle	Mesopore vol loss[a] (%)	TiO_2 content[b] (wt%)	Mesopore vol loss per ALD cycle[c] (%)	TiO_2 gain per ALD cycle[d] (wt%)	Ratio of mesopore vol loss/TiO_2 weight gain[e]
PMFI	1	1.92	0.23	1.92	0.23	8.36
	5	7.05	0.80	1.41	0.16	8.81
PMWW	1	12.44	0.61	12.44	0.61	20.39
	5	16.10	0.88	3.22	0.18	18.19

[a] Calculated from mesopore volume data Table 1.
[b] Determined by ICP-OES.
[c] Calculated by division of mesopore volume loss by the number of ALD cycles.
[d] Calculated by division of TiO_2 content by the number of ALD cycle; [e] Calculated by division of mesopore volume loss per ALD cycle by TiO_2 weight gain per ALD cycle.

of mesopore volume loss to TiO_2 weight gain after the first and fifth ALD cycles was calculated, which depends on the type of zeolite (8.36 in PMFI-ALD-1 and 8.81 in PMFI-ALD-5 versus 20.39 in PMWW-ALD-1 and 18.19 in PMWW-ALD-5), not obviously on the number of ALD cycles. The same loading amount of TiO_2 caused ~2.5 times higher volume loss in PMWW than that in PMFI.

On the basis of above analyses, the following differences in mesopore characteristics between PMFI and PMWW can be pictured. First of all, the communication in the mesopore network in PMFI is better than in PMWW. This is indicated by the nearly constant volume loss and weight gain in PMFI and significantly lower volume loss and weight gain in PMWW, respectively, with increasing number of ALD cycle. The good mesopore network communication onto PMFI guaranteed the entry and exit of TTIP molecules and byproducts from ALD surface reactions in pulsing and purging steps, respectively, which led to a steady state growth of TiO_2 with increasing number of ALD cycles. On the other hand, the entrance or certain location in the mesopore network in PMWW might be blocked after one ALD cycle of TiO_2 which prevented the further deposition of TTIP into the substrate in the following ALD cycles. Secondly, the size of mesopore entrance in PMWW is smaller than that of PMFI, which is indicated by the nearly three times higher TiO_2 loading in PMWW-ALD-1 than PMFI-ALD-1. As described in the experimental section, the N_2 purge was followed after TTIP dosing before the zeolite material was exposed to water. The physical trap of TTIP in mesopores and subsequent high TiO_2 deposition due to pore entrance blockage after the TTIP exposure in PMFI with uniform pore sizes (from entrance to pore body) was hardly to happen. However, the trap of TTIP in mesopores due to delay in emptying pore body could occur if the pore neck size is smaller than pore body, similar to the phenomenon of hysteresis loop in Ar adsorption-desorption isotherms. The isotherm data in Figs. 4 and 5 shows that hysteresis loop (width and closing point) has more obvious change after TiO_2 ALD in PMWW, consistent with analysis for high TiO_2 loading in PMWW-ALD-1 sample. Thirdly, the direct communication between micropore within and mesopore between zeolitic layers in PMFI than PMWW is different. As shown by the last entry in Table 3, PMWW has a high mesopore volume loss/TiO_2 weight gain ratio, nearly 2.5 times higher than PMFI. Both PMFI and PMWW have hierarchical micro- and mesoporosity. Even if the mesopore entrance was blocked by TiO_2, adsorptive molecule, either Ar or N_2 in isotherm measurement, still can access to mesopores via micropore in zeolitic layer since they are not influenced by the ALD process. Therefore, the mesopore volume loss per unit mass of deposited TiO_2 should be comparable. Apparently, PMFI has much better channel connection beween micro- and mesopores than PMWW zeolite.

The different mesopore characteristics in PMFI and PMWW may result from the different topological structures of zeolitic layers and pillars in both zeolites. As discussed in previous work [53–55], MFI zeolite consists of two interconnected 10-MR channel systems: one is straight running along the b-axis direction (0.53 × 0.56 nm) and the other is zigzag running parallel to the a-axis direction (0.51 × 0.55 nm). The mesopores in PMFI is parallel to the zigzag channels and perpendicular to the straight channels within the layers. A direct communication between straight 10-MR channel in zeolitic layer and mesopore between two adjacent layers (shown in Fig. 6(A)–(C)) is expected. MWW structure contains two independent micropore systems: one is defined by sinusoidal 10-MR channels with dimensions of 0.41 × 0.51 nm and the other one consists of supercages delimited by 12-MR channels with dimensions of 0.71 × 0.71 × 1.81 nm. The consecutive supercages are connected through slightly distorted elliptical 10-MR windows (0.40 × 0.55 nm). The mesopores in PMWW parallels with the 10-MR sinusoidal channels and normal to hourglass shaped pores (surface cups in PMWW), as presented in Fig. 6(D)–(F). The direct communication between micropore in zeolitic layer and mesopores between layers is restricted by the 6-MR neck between two bulbs of the hourglass shape micropores. In addition, the connection between the surface cups from both adjacent zeolitic layers with mesopore between zeolitic layers is naturally realized, which enlarges the mesopore size normal to zeolite layer direction and tortures the running direction of mesopores in PMWW zeolite, as indicated by the schematic structure in Fig. 6(E). The intact mesopore sizes after TiO_2 ALD in Figs. 4(C) and 5(B) should mainly result from the contribution of the surface cups in zeolitic layers.

The distribution of pillars (or mesopores) in the gallery space of PMFI and PMWW can be different from the understanding of the materials preparation process. As discussed in the experimental section, PMWW was prepared from the swollen MCM-22(P) that contained organic CTAB surfactant introduced by post-modification process to keep zeolite layers apart [32,56]. The organic swelling agent was introduced after MCM-22(P) formation, which might not be uniformly distributed from perimeter to the center of the flake-like particles. It might be realistic to imagine that the concentration of CTAB molecules between zeolitic layers decreases from perimeter to the center due to diffusion limitation. However, PMFI was made from multilamellar MFI that has $C_{22\text{-}6\text{-}6}$ surfactant between zeolite layers and built from the beginning of hydrothermal crystallization process [26]. The self-assembly of $C_{22\text{-}6\text{-}6}$ and zeolite synthetic gel is desirable to predict that the organic spacer is uniform in the entire gallery space between zeolite layers. The TGA data in Fig. S4 shows that multilamellar MFI contains ~22 wt% more surfactant molecules than that of swollen MCM-22(P). Therefore, more uniform mesopores are formed in PMFI compared to PMWW after the removal of organic surfactant spacers by calcination. Thus, the mesopore morphology in PMFI and PMWW zeolites are extrapolated from above discussions and shown in Fig. 6(C) and (F), respectively.

JEOL JEM-2100 FEG Scanning Transmission Electron Microscopy (STEM) with a High-Angle Annular Dark Field detector (HAADF) was used to study the location of TiO_2 in PMFI and PMWW zeolites after the five cycles of TiO_2 ALD. The representative STEM-HAADF images are shown in Figs. S5–S6. Features attributable to multiple parallel stacking MFI layers are observed in Fig. S5, indicating that the layered structure was preserved after the TiO_2 ALD treatment of the pristine PMFI sample. In comparison to the pristine PMFI sample, the PMFI-ALD-5 has many bright spots distribute primarily between two zeolitic layers. This indicates the presence of the TiO_2 and their location in the PMFI-ALD-5 sample. The layered structure is also observed in PMWW zeolite, either prior to or after, the ALD-TiO_2 treatment (Fig. S6). Similar to that of PMFI-ALD-5 sample, the PMWW-ALD-5 is brighter than PMWW. The number of linkages between two zeolitic layers in PMWW-ALD-5 is much higher than that of PMWW. Different from PMFI-ALD-5 sample, the TiO_2 seems to stay near the surface of mesoporous gallery (i.e., pore entrance) in PMWW-ALD-5. This reflects the difference in mesopore communication between PMFI and PMWW zeolites, as discussed from the composition and isotherm analysis above.

3.5. Coordination environment of Ti-species in TiO_2 ALD modified PMFI and PMWW zeolites

The DR UV–Vis spectra, shown in Fig. 7, were measured on PMFI and PMWW zeolites before and after ALD-TiO_2 process, respectively, to identify the coordination environment of Ti-species. For comparison, the DR UV–Vis spectra of Aeroxide® P25 titania and titanosilicalite-1 (TS-1) zeolite are measured at the same conditions and included in Fig. 7. The absence of obvious absorption band in PMFI and PMWW zeolite is consistent with the absence of Ti-species in both samples. The framework Ti-species in TS-1 result in an obvious absorption band centred at ~211 nm, which is assigned to the charge transfer from O^{2-} to Ti^{4+} in the tetrahedral (T_d) framework Ti-sites [57,58]. The Aeroxide® P25 exhibits an absorption band at ~ 307 nm that is assigned to the charge transfer from O^{2-} to Ti^{4+} in an octahedral (O_h) coordination in titania phase. The peak at 256 nm is attributed to the extra-framework Ti sites according to previous report [58]. The deposition of Ti-species by ALD-TiO_2 process onto PMFI and PMWW zeolites led to a

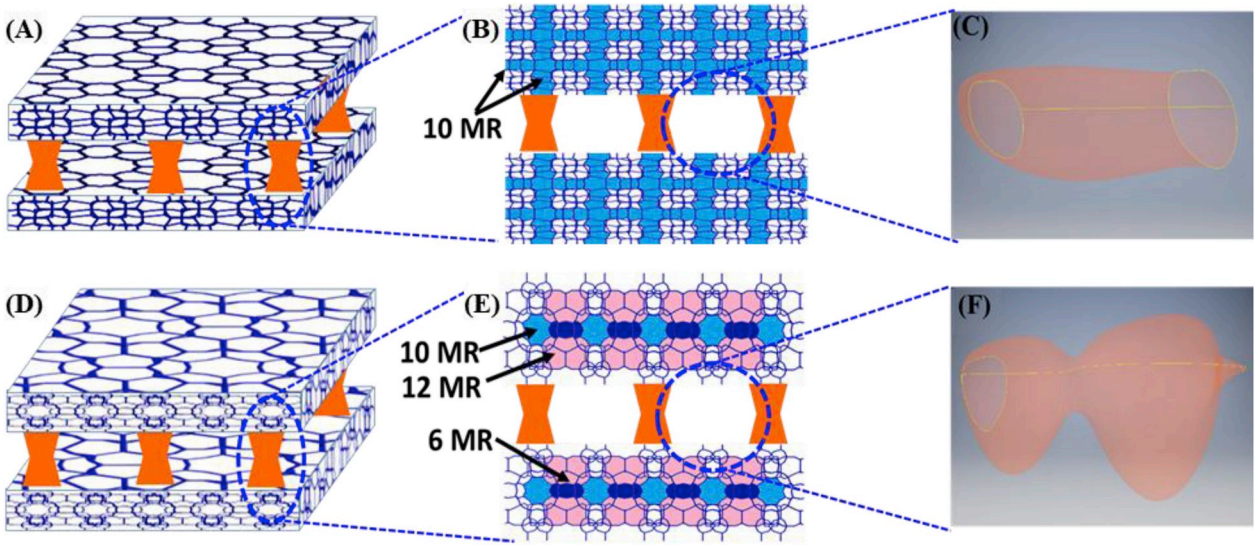

Fig. 6. Schematic illustration of PMFI (A) and PMWW (D) zeolite with micro- and mesopore network between 2D zeolitic layers. (B) and (E) are cross-sectional view of pore entrance of mesopore network, (C) and (F) are the perspective view of mesoporous channels in PMFI and PMWW zeolites, respectively.

broad DR UV–vis peak in Fig. 7, indicating the presence of Ti-sites with various bonding situations in the materials. First of all, a strong peak cantered at 211 nm with a shoulder at 256 nm is observed in PMFI-ALD-1 sample, which suggests the presence of framework Ti-sites accompanied with the extra-framework Ti-sites and titania structure. The increase in ALD cycles enhanced the intensity of the shoulder peak in PMFI-ALD-5, meaning the increase in the number of extra-framework and titania sites. Different from PMFI-based zeolite, the PMWW-ALD-1 has the DR UV–vis peak centred at 232 nm. This indicated the less number of framework Ti sites compared to extra-framework positions in this material. The increase in ALD cycles enhanced the should peak, meaning more TiO_2 materials deposited as the extra-framework and titania phase. Surprisingly, the zeolite substrate induced the epitaxial growth of Ti-sites to form framework structure in the initial ALD-TiO_2 process, and PMFI has strong templating effect than PMWW in this growth. Still, the titania phase was formed with high number of ALD cycles, but still, the formed titania was in PMFI and PMWW zeolites too small to be distinguished by the XRD measurement.

3.6. Photocatalytic tests on ALD-TiO_2 modified PMFI and PMWW zeolites

It is known that titania is photo-responsive catalyst for photocatalytic reactions [15,59]. The introduction of titania onto 2D zeolites by TiO_2 ALD could enable photocatalytic activity of pillared lamellar 2D zeolites for photocatalysis applications. Two different reactions, MO decomposition and CO_2 reduction, were therefore studied to understand the performance of titania-modified PMFI and PMWW zeolites in photocatalytic environment remedy reactions.

The decomposition of MO was conducted in an aqueous solution to examine the photocatalytic capability of the as-produced PMFI-ALD-1, PMFI-ALD-5, PMWW-ALD-1 and PMWW-ALD-5 samples. The conversion, i.e, degradation degree (η), of MO was defined by $\eta = (C_0 - C)/C_0 \times 100\%$, where C_0 and C are the concentrations of MO (g L^{-1}) in the beginning of the reaction and at local reaction time, respectively. The degradation degree versus reaction time followed the pseudo-first order kinetic behavior. Fig. 8(A) shows the rate constants of MO decomposition evaluated for PMFI and PMWW after TiO_2 ALD. PMFI and PMWW did not exhibit any photocatalytic activity due to the absence of Ti sites in the samples. PMFI-ALD-1 has higher rate constant than PMFI-ALD-5, which should be due to lower areal active site density and higher number of framework Ti-sites [60,61]. The same trend was observed between PMWW-ALD-1 and PMWW-ALD-5 samples. For comparison, the state-of-the-art titania photocatalyst, Aeroxide® P25, has much (~12 times) lower activity than that of TiO_2 ALD modified PMFI and PMWW zeolites. The higher surface area of zeolite samples led to lower areal Ti-site density that should be directly correlated to the per active site activity differences between zeolite-based photocatalysts and Aeroxide® P25 titania [15].

To further demonstrate the photocatalytic capability of TiO_2 ALD modified PMFI and PMWW zeolites, the photocatalytic reduction of

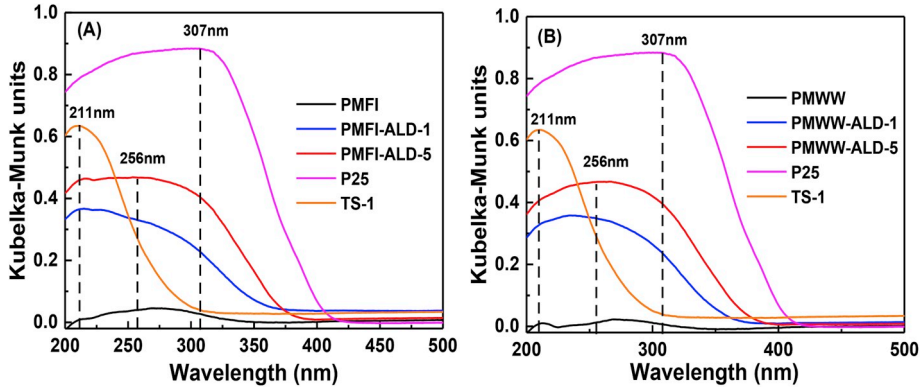

Fig. 7. Diffuse reflectance (DR) UV–vis spectra of PMFI, PMFI-ALD-1 and PMFI-ALD-5 (A), PMWW, PMWW-ALD-1 and PMWW-ALD-5 (B), respectively. DR UV–vis of Aeroxide® P25 and TS-1 are used for comparison in both figures.

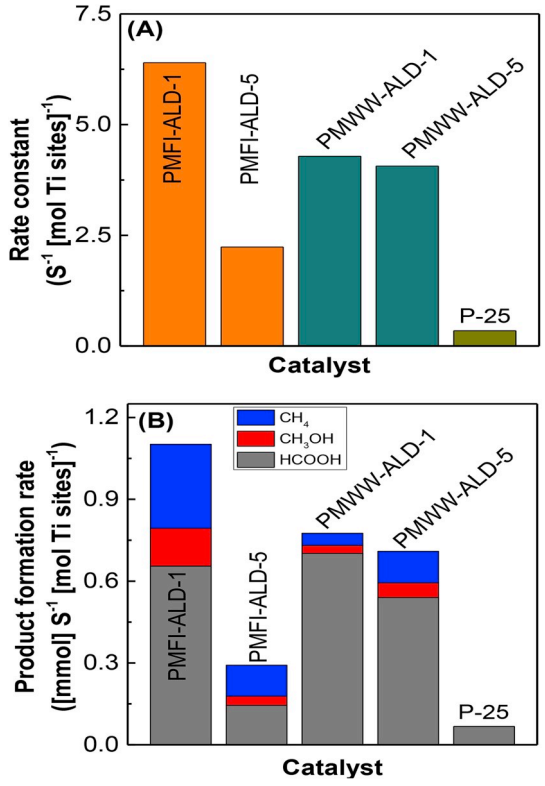

Fig. 8. Photocatalytic MO degradation (A) and CO_2 reduction (B) reactions over PMFI-ALD-1, PMFI-ALD-5, PMWW-ALD-1, PMWW-ALD-5 zeolite samples. The same reactions over Aeroxide® P25 were included for comparison purpose.

CO_2 with water was examined. PMFI and PMWW did not show any photocatalytic activity, while ALD-TiO_2 modified PMFI-ALD-1, PMFI-ALD-5, PMWW-ALD-1 and PMWW-ALD-5 samples were photocatalytically active for CO_2 reduction reaction (Fig. 8(B)). Similar to that in MO decomposition reaction, PMFI-ALD-1 and PMWW-ALD-1 samples have much higher activity than that of PMFI-ALD-5 and PMWW-ALD-5 samples. All of the zeolite-based photocatalysts have much higher activity (> 10 times) than the commercial Aeroxide® P25 titania. Methane (CH_4), methanol (CH_3OH) and formic acid (HCOOH) were detected products in the reaction. PMFI-ALD-1 and PMFI-ALD-5 have higher oxygenated hydrocarbon product (methanol and formic acid) selectivity than PMWW-ALD-1 and PMWW-ALD-5 samples. This might be due to the more hydrophilic nature of PMFI zeolite since it has ~8 times higher silanol groups per unit-cell volume than PMWW zeolite [24]. The absence of hydrocarbon oxygenate product in Aeroxide® P25 might be due to the different coordination environment of Ti-sites in titania compared to that in PMFI and PMWW-based zeolites, as indicated by the DR UV–vis spectra in Fig. 7.

4. Conclusions

In summary, the combination of TiO_2 ALD with structural, textural, compositional and catalytic analyses of PMFI and PMWW zeolites, prior to and afterwards, were employed to study the mesopore differences in PMFI and PMWW zeolites for the first time. Although both PMFI and PMWW share many similar topological features in pillared lamellar zeolites, they have quite different mesopore characteristics. PMFI has uniform mesopores that have good communication between pore entrance and main body as well as to micropores within zeolitic layers. PMWW, however, has non-uniformity in mesopore sizes, small pore entrance and large pore body, as well as inconvenient communication within the mesopore network and no communication to micropore in zeolitic layers. These mesopore differences result from different topological structure of zeolitic layer and pillars between layers in PMFI and PMWW zeolites. The post-modification process for preparation of PMWW precursor and bottom-up synthesis of PMFI precursor materials were speculated to directly impact the mesopore uniformity and connections. The TiO_2 ALD introduced photocatalytically active materials into 2D lamellar zeolites, which enabled new application of these materials, sustainable catalysts for environmental remedy reactions.

Acknowledgements

The authors gratefully acknowledge financial support from National Science Foundation (NSF-CBET 1705284, 1642405, 1264599 and 1351384). We acknowledge the support of Maryland NanoCenter and its AIMLab. The AIMLab is supported in part by the NSF as a MRSEC Shared Experimental Facility. This material is based upon work supported by, or in part by, the U. S. Army Research Laboratory and the U. S. Army Research Office under contract/grant number: W911NF-17-1-0363. Zheng Lu and Yu Lei thank the support from NSF CBET-1511820. Zhenglong Li is supported by the BioEnergy Technologies Office, Office of Energy Efficiency and Renewable Energy, U.S. Department of Energy, under contract DE-AC05-00OR22725 with UT-Battelle, LLC.

Appendix A. Supplementary data

Supplementary information available: Materials and procedure for synthesis of PMFI and PMWW zeolites, Ar and N_2 isotherms, pore size distributions calculated from the adsorption and desorption branches of Ar isotherms, pore size distributions evaluated from the desorption branches of Ar and N_2 isotherms, as well as TGA data for quantification of organic contents in precursors of PMFI and PMWW zeolites.

Supplementary data to this article can be found online at https://doi.org/10.1016/j.micromeso.2018.10.009.

References

[1] W.J. Roth, B. Gil, W. Makowski, B. Marszalek, P. Eliášová, Chem. Soc. Rev. 45 (2016) 3400–3438.
[2] U. Diaz, A. Corma, Dalton Trans. 43 (2014) 10292–10316.
[3] Y. Wei, T.E. Parmentier, K.P. de Jong, J. Zecevic, Chem. Soc. Rev. 44 (2015) 7234–7261.
[4] S. Mitchell, A.B. Pinar, J. Kenvin, P. Crivelli, J. Karger, J. Perez-Ramirez, Nat. Commun. 6 (2015) 14.
[5] A. Corma, V. Fornes, J. Martınez-Triguero, S. Pergher, J. Catal. 186 (1999) 57–63.
[6] A. Corma, V. Fornes, S. Pergher, T.L. Maesen, J. Buglass, Nature 396 (1998) 353–356.
[7] K. Varoon, X. Zhang, B. Elyassi, D.D. Brewer, M. Gettel, S. Kumar, J.A. Lee, S. Maheshwari, A. Mittal, C.-Y. Sung, Science 334 (2011) 72–75.
[8] K.V. Agrawal, B. Topuz, Z. Jiang, K. Nguenkam, B. Elyassi, L.F. Francis, M. Tsapatsis, M. Navarro, AIChE J. 59 (2013) 3458–3467.
[9] S. Sabnis, V.A. Tanna, C. Li, J. Zhu, V. Vattipalli, S.S. Nonnenmann, G. Sheng, Z. Lai, H.H. Winter, W. Fan, Chem. Commun. 53 (2017) 7011–7014.
[10] I. Ogino, M.M. Nigra, S.-J. Hwang, J.-M. Ha, T. Rea, S.I. Zones, A. Katz, J. Am. Chem. Soc. 133 (2011) 3288–3291.
[11] C. Kresge, W. Roth, K. Simmons, J. Vartuli, US Patent 5,229,341 (1993), (Assigned to Mobil Oil).
[12] Kresge, C.T., Roth, W.J., Simmons, K.G. and Vartuli, J.C. Crystalline oxide material. U.S. Patent 5,250,277, 1993.
[13] S. Maheshwari, C. Martínez, M. Teresa Portilla, F.J. Llopis, A. Corma, M. Tsapatsis, J. Catal. 272 (2010) 298–308.
[14] K. Na, M. Choi, W. Park, Y. Sakamoto, O. Terasaki, R. Ryoo, J. Am. Chem. Soc. 132 (2010) 4169–4177.
[15] L. Emdadi, D.T. Tran, J. Zhang, W. Wu, H. Song, Q. Gan, D. Liu, RSC Adv. 7 (2017) 3249–3256.
[16] B. Liu, C. Wattanaprayoon, S.C. Oh, L. Emdadi, D. Liu, Chem. Mater. 27 (2015) 1479–1487.
[17] M. Shete, M. Kumar, D.H. Kim, N. Rangnekar, D.D. Xu, B. Topuz, K.V. Agrawal, E. Karapetrova, B. Stottrup, S. Al-Thabaiti, S. Basahel, K. Narasimharao, J.D. Rimer, M. Tsapatsis, Angew. Chem. Int. Ed. 56 (2017) 535–539.
[18] N. Rangnekar, M. Shete, K.V. Agrawal, B. Topuz, P. Kumar, Q. Guo, I. Ismail, A. Alyoubi, S. Basahel, K. Narasimharao, C.W. Macosko, K.A. Mkhoyan, S. Al-Thabaiti, B. Stottrup, M. Tsapatsis, Angew. Chem. Int. Ed. 54 (2015) 6571–6575.
[19] A. Corma, U. Diaz, M.E. Domine, V. Fornés, J. Am. Chem. Soc. 122 (2000) 2804–2809.
[20] A. Corma, U. Díaz, T. García, G. Sastre, A. Velty, J. Am. Chem. Soc. 132 (2010)

15011–15021.
[21] M. Opanasenko, W.O. Parker Jr., M. Shamzhy, E. Montanari, M. Bellettato, M. Mazur, R. Millini, J. Cejka, J. Am. Chem. Soc. 136 (2014) 2511–2519.
[22] U. Díaz, ISRN Chem. Eng. 2012 (2012) 35.
[23] D. Liu, A. Bhan, M. Tsapatsis, S. Al Hashimi, ACS Catal. 1 (2010) 7–17.
[24] D. Liu, X. Zhang, A. Bhan, M. Tsapatsis, Microporous Mesoporous Mater. 200 (2014) 287–290.
[25] Y. Wu, L. Emdadi, Z. Wang, W. Fan, D. Liu, Appl. Catal. 470 (2014) 344–354.
[26] M. Choi, K. Na, J. Kim, Y. Sakamoto, O. Terasaki, R. Ryoo, Nature 461 (2009) 246–249.
[27] Kresge, Charles T., and Wieslaw J. Roth. Method for preparing a pillared layered oxide material. U.S. Patent 5,278,115, Jan 11, 1994.
[28] X. Zhang, D. Liu, D. Xu, S. Asahina, K.A. Cychosz, K.V. Agrawal, Y. Al Wahedi, A. Bhan, S. Al Hashimi, O. Terasaki, M. Thommes, M. Tsapatsis, Science 336 (2012) 1684–1687.
[29] S.M. George, Chem. Rev. 110 (2010) 111–131.
[30] B.J. O'Neill, D.H.K. Jackson, J. Lee, C. Canlas, P.C. Stair, C.L. Marshall, J.W. Elam, T.F. Kuech, J.A. Dumesic, G.W. Huber, ACS Catal. 5 (2015) 1804–1825.
[31] J. Lu, J.W. Elam, P.C. Stair, Acc. Chem. Res. 46 (2013) 1806–1815.
[32] S. Maheshwari, E. Jordan, S. Kumar, F.S. Bates, R.L. Penn, D.F. Shantz, M. Tsapatsis, J. Am. Chem. Soc. 130 (2008) 1507–1516.
[33] Y. Wu, Z. Lu, L. Emdadi, S.C. Oh, J. Wang, Y. Lei, H. Chen, D.T. Tran, I.C. Lee, D. Liu, J. Catal. 337 (2016) 177–187.
[34] Z. Lu, M. Piernavieja-Hermida, C.H. Turner, Z. Wu, Y. Lei, J. Phys. Chem. C 122 (2018) 1688–1698.
[35] W.J.K. Roth, C. T, J.C. Vartuli, M.E. Leonowicz, A.S. Fung, S.B. McCullen, H.G.K.H.K. Beyer, I. Kiricsi, J.B. Nagy (Eds.), Catalysis by Microporous Materials, Studies in Surface Science and Catalysis, Elsevier, Amsterdam, 1995, pp. 301–308.
[36] M. Thommes, K.A. Cychosz, Adsorption 20 (2014) 233–250.
[37] M. Thommes, K. Kaneko, A.V. Neimark, J.P. Olivier, F. Rodriguez-Reinoso, J. Rouquerol, K.S. Sing, Pure Appl. Chem. 87 (2015) 1051–1069.
[38] K.A. Cychosz, R. Guillet-Nicolas, J. García-Martínez, M. Thommes, Chem. Soc. Rev. 46 (2017) 389–414.
[39] E. Verheyen, S. Pulinthanathu Sree, K. Thomas, J. Dendooven, M. De Prins, G. Vanbutsele, E. Breynaert, J.P. Gilson, C.E.A. Kirschhock, C. Detavernier, J.A. Martens, Chem. Commun. (Camb). 50 (2014) 4610–4612.
[40] F. Wang, W.Y. Xiao, G.M. Xiao, Catal. Lett. 145 (2015) 860–867.
[41] H. Vuori, R.J. Silvennoinen, M. Lindblad, H. Österholm, A.O.I. Krause, Catal. Lett. 131 (2009) 7–15.
[42] C. Detavernier, J. Dendooven, S. Pulinthanathu Sree, K.F. Ludwig, J.A. Martens, Chem. Soc. Rev. 40 (2011) 5242–5253.
[43] J. Dendooven, B. Goris, K. Devloo-Casier, E. Levrau, E. Biermans, M.R. Baklanov, K.F. Ludwig, P.V.D. Voort, S. Bals, C. Detavernier, Chem. Mater. 24 (2012) 1992–1994.
[44] A. Zukal, M. Kubu, Dalton Trans. 43 (2014) 10558–10565.
[45] M. Thommes, B. Smarsly, M. Groenewolt, P.I. Ravikovitch, A.V. Neimark, Langmuir 22 (2006) 756–764.
[46] J.C. Groen, L.A.A. Peffer, J. Pérez-Ramírez, Microporous Mesoporous Mater. 60 (2003) 1–17.
[47] S.H. Keoh, W. Chaikittisilp, A. Endo, A. Shimojima, T. Okubo, Bull. Chem. Soc. Jpn. 90 (2017) 586–594.
[48] N. Koike, W. Chaikittisilp, A. Shimojima, T. Okubo, RSC Adv. 6 (2016) 90435–90445.
[49] Y. He, G. Nivarthy, F. Eder, K. Seshan, J. Lercher, Microporous Mesoporous Mater. 25 (1998) 207–224.
[50] W.J. Roth, C.T.K, K.G. Simmons, J.C. Vartuli WO Patent 92/011935, 1992.
[51] Y. Tao, H. Kanoh, L. Abrams, K. Kaneko, Chem. Rev. 106 (2006) 896–910.
[52] P.L. Llewellyn, J.P. Coulomb, Y. Grillet, J. Patarin, G. Andre, J. Rouquerol, Langmuir 9 (1993) 1852–1856.
[53] Y. He, T.C. Hoff, L. Emdadi, Y. Wu, J. Bouraima, D. Liu, Catal. Sci. Technol. 4 (2014) 3064–3073.
[54] S.C. Oh, T. Nguyendo, Y. He, A. Filie, Y. Wu, D.T. Tran, I.C. Lee, D. Liu, Catal. Sci. Technol. 7 (2017) 1153–1166.
[55] W. Makowski, K. Mlekodaj, B. Gil, W.J. Roth, B. Marszalek, M. Kubu, P. Hudec, A. Smieskova, M. Hornacek, Dalton Trans. 43 (2014) 10574–10583.
[56] J.-O. Barth, A. Jentys, J. Kornatowski, J.A. Lercher, Chem. Mater. 16 (2004) 724–730.
[57] G. Ricchiardi, A. Damin, S. Bordiga, C. Lamberti, G. Spanò, F. Rivetti, A. Zecchina, J. Am. Chem. Soc. 123 (2001) 11409–11419.
[58] H.L. Chen, S.W. Li, Y.M. Wang, J. Mater. Chem. 3 (2015) 5889–5900.
[59] J. Schneider, M. Matsuoka, M. Takeuchi, J. Zhang, Y. Horiuchi, M. Anpo, D.W. Bahnemann, Chem. Rev. 114 (2014) 9919–9986.
[60] T. Ban, S. Kondoh, Y. Ohya, Y. Takahashi, Phys. Chem. Chem. Phys. 1 (1999) 5745–5752.
[61] G.D. Lee, S.K. Jung, Y.J. Jeong, J.H. Park, K.T. Lim, B.H. Ahn, S.S. Hong, Appl. Catal., A 239 (2003) 197–208.

Supplementary Information for

Mesopore Differences between Pillared Lamellar MFI and MWW Zeolites Probed by Atomic Layer Deposition of Titania and Consequences on Photocatalysis

Junyan Zhang[a], Zheng Lu[b], Wei Wu[a], Dat T. Tran[c], Wenjin Shang[d], Huiyong Chen[d], Yu Lei[b], Zhenglong Li[e], Mei Wang[a], Taylor J. Woehl[a] and Dongxia Liu[a*]

[a] Department of Chemical and Biomolecular Engineering, University of Maryland, College Park, MD, 20742, USA

[b] Department of Chemical and Materials Engineering, University of Alabama in Huntsville, Huntsville, AL, 35899, USA

[c] U. S. Army Research Laboratory, RDRL-SED-E, 2800 Powder Mill Road, Adelphi, MD, 20783, USA

[d] School of Chemical Engineering, Northwest University, Xi'an, Shanxi, 710069, China

[e] Energy & Transportation Sciences Division, Oak Ridge National Laboratory, Oak Ridge, TN, 37831, USA

*Corresponding author:
Prof. Dongxia Liu
Email: liud@umd.edu

S1. Experimental

S1.1. Materials

Tetraethyl orthosilicate (TEOS, 98%), sodium hydroxide (NaOH, ≥ 97.0%), sulfuric acid (H_2SO_4, 95.0-98.0%), sodium aluminate ($NaAlO_2$, ≥ 99.05 %), fumed silica (SiO_2, 99.8%), ammonium nitrate (NH_4NO_3, ≥99.0%), hexamethyleneimine ($C_6N_{13}N$, HMI, ≥95.0%), tetrapropylammonium hydroxide solution (40%), titanium isopropoxide (TTIP, 99.999%), titanium (IV) oxide (Aeroxide® P25 titania, ≥99.5% trace metal basis) and methyl orange (MO, 85% dye content) were all purchased from Sigma-Aldrich. Aluminum sulfate hydrate ($Al_2(SO_4)_3 \cdot 16H_2O$, 99%) was supplied by Mallinckrodt Chemicals. Cetyltrimethylammonium bromide (CTAB) was bought from Alfa Aesar. Deionized (DI) water was used throughout the experiment. Diquaternary ammonium surfactant ($[C_{22}H_{45}\text{-}N^+(CH_3)_2\text{-}C_6H_{12}\text{-}N^+(CH_3)_2\text{-}C_6H_{13}]Br_2^-$, ($C_{22\text{-}6\text{-}6}$)) was synthesized based on the reported method[1] and the synthesis procedure has also been explained in our previous publications[2,3].

S1.2. Synthesis of PMFI and PMWW zeolites

Synthesis of PMFI zeolite. The PMFI zeolite was synthesized from the multilamellar MFI precursor, which was prepared following the recipe reported by Choi et al.[1] In the synthesis, 8.0 g NaOH was dissolved in 35.1 g DI water to form the basic solution A. 2.7 g H_2SO_4 was added into 48.0 g DI water to form the acidic solution B. Then, the basic solution A was added dropwise to the acidic solution B under vigorously magnetic stirring. Afterwards, 1.2 g $Al_2(SO_4)_3 \cdot 16H_2O$ was added, followed by addition of 37.6 g TEOS. The resultant mixture was stirred vigorously at room temperature for 24 h. Meanwhile, 13.1 g $C_{22\text{-}6\text{-}6}$ was dissolved in 90.0 g DI water at 333 K to form a clear surfactant template solution. After addition of the $C_{22\text{-}6\text{-}6}$ surfactant solution, the

mixture was continuously stirred for 2 h. Finally, the resultant zeolite synthetic gel was split equally into six portions, and transferred into six corresponding Teflon-lined stainless-steel autoclaves. The autoclaves were tumbled vertically at 30 rpm and 423 K for 5 days for synthesis of multilamellar MFI zeolite. Lastly, the zeolite sample was collected by centrifugation, washing with DI water, and dring at 343 K overnight.

The synthesis of PMFI was carried out by dispersing the multilamellar MFI in a TEOS solvent at a weight ratio of TEOS to zeolite of 5. The multilamellar MFI/TEOS suspension was then sealed in a flask and heated in an oil bath at 351 K for 24 h under the argon (Ar) atmosphere. The zeolite sample was collected by centrifugation at 6500 rpm for 30 min. After drying at room temperature overnight, the sample was hydrolyzed in an NaOH aqueous solution (pH = 8). The weight ratio of aqueous solution to solid sample was controlled at 10. After stirring the hydrolyzing suspension in an oil bath at 313 K for 6 h, the zeolite sample was collected by centrifugation, washed with DI water, and then dried under ambient condition. Finally, the sample was heated to 723 K for 6 h under N_2 atmosphere (flow rate =100 mL min^{-1}) and then under flowing air atmosphere (flow rate = 100 mL min^{-1}) at 823K for 12 h. To synthesize the proton-form (H^+ form) PMFI, the calcined sample was ion-exchanged for three times with 1 M aqueous NH_4NO_3 solution at 353 K for 12 h. The weight ratio of NH_4NO_3 solution to zeolite equaled to 10. Subsequently, the ion-exchanged sample was collected by centrifugation, washed with DI water, and dried at 343 K for 12 h. The second calcination was applied to the sample at 823 K for 6 h in flowing air (flow rate = 100 mL min^{-1}) to decompose the NH_4^+ cations in ion-exchanged PMFI zeolite into form the H^+ and NH_3.

Synthesis of PMWW zeolite. The PMWW was synthesized following the method reported by Maheshwari et al.[4] by pillaring the precursor MCM-22(P) with TEOS. The synthesis of

MCM-22(P) was conducted by dissolving 1.3 g NaOH in 233.1 g DI water, followed by addition of 1.37g $NaAlO_2$ under magnetic stirring to form a clear solution. 14.3 g of HMI and 17.7 g of fumed SiO_2 were added into above solution to form a mixture and the mixture was stirred for 24 h to form a homogeneous zeolite synthetic gel. Afterwards, the gel was spliced into six portions and transferred into six autoclaves, respectively. The same set-up as that of multilamellar MFI was used for synthesis of MCM-22(P) except that the synthesis temperature was controlled at 308 K for 11 days. The zeolite product was centrifuged at 6500 rpm for 30 min and washed with DI water until pH=9. Finally, a MCM-22(P) wet cake was obtained for the next synthesis steps for preparation of PMWW zeolite.

Swelling of MCM-22(P) was firstly carried out for preparation of PMWW zeolite. 20.0 g MCM-22(P) wet cake was mixed with 22.5g CTAB, 24.4 g TPAOH solution (40%) and 55.0g DI water in a plastic container. The mixture was stirred at room temperature for 10 h. The zeolite sample was then collected by centrifugation at 6500 rpm for 0.75 h. After this, the sample was washed with 200 mL DI water for 0.5 h. The centrifugation and water washing steps were repeated alternatively for 30 times. Finally, the swollen MCM-22(P) sample was dried at room temperature overnight. The pillaring of swollen MCM-22(P) was done using the same procedures as those of PMFI. An ion-exchange procedure was also applied to PMWW to make for proton-form zeolite prior to the ALD modification processes.

S1.3. Photocatalytic reactions over ALD-TiO_2 modified PMFI and PMWW zeolites

Photocatalytic decomposition of MO molecules. To test the photocatalytic performance of ALD-Ti modified PMFI and PMWW zeolites, the liquid phase catalytic degradation of MO molecules under light irradiation was employed. A 200 W HBO Mercury (Hg) lamp (OSRAM,

Germany) was chosen as the light source, which was located 15 cm away from the reactor. A 100 mL quartz flask was employed as the reactor for the MO solution. In the photocatalytic reaction, 0.02 g of zeolite sample was mixed with 20 mL MO solution with concentration of 0.1g L^{-1} in the flask. After stirring for 4 h under darkness condition, 1 mL of liquid sample was taken and the lamp was turned on. This moment of turning on the Hg lamp was recorded as time of 0 h. Liquid samples were withdrawn at 1 hour intervals and MO decomposition was analyzed by a Lambda 40 UV/Vis spectrophotometer (PerkinElmer Instruments).

Photocatalytic reduction of CO_2. To further evaluate the photocatalytic performance of ALD-Ti modified PMFI and PMWW zeolites, the CO_2 reduction reaction was performed in a cylindrical batch reactor under ambient conditions. The batch reactor was composed mainly of a stainless steel body and two quartz windows of 3 cm in diameter. The internal volume and the depth of the batch reactor were 14 mL and 3 cm, respectively. Two gas connection lines (inlet and outlet of the reactor) stayed opposite to each other on the perimeter wall of the cylindrical reactor body. In the experiment, 0.02 g zeolite and 0.05 mL water were charged into the reactor and were treated in a gas mixture of 42 mL min^{-1} CO_2 and 9 mL min^{-1} Ar for 50 min prior to the reaction. After turning off the shut-off valves located at inlet and outlet of the reactor, a Xenon lamb(450W) was applied to the reactor through the quartz window located on the top of the reactor. After 4 h of irradiation, the Xe lamp was turned off and the gas mixture in the reactor was analyzed by a gas-chromatography (Agilent Technologies, 6890N) through an automated gas valve. A3.0m×1/8inch packed column (Agilent HAYESEP DB) and a 30 m×0.25 mm capillary column (Supelco SP-2330) which were connected to a thermal conductivity detector and a flame ionization detector, respectively, were used to calibrate and separate the reactants and products.

S2. Morphology of PMFI and PMWW zeolites before and after TiO_2 ALD

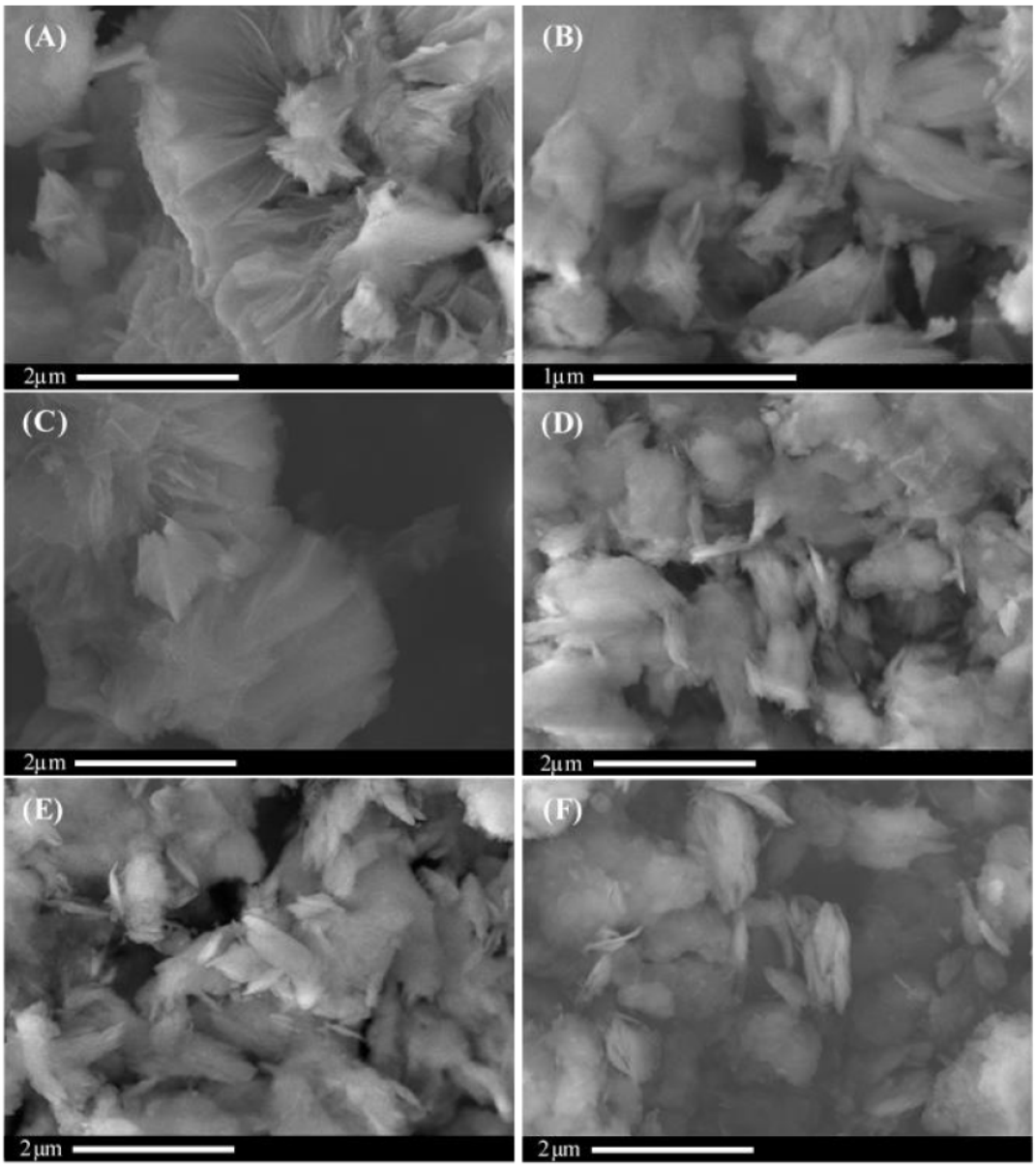

Fig. S1. SEM images showing morphologies of PMFI (A), PMFI-ALD-1 (B), PMFI-ALD-5 (C), PMWW (D), PMWW-ALD-1 (E), and PMWW-ALD-5 (F), respectively. (Scale bar in each figure is 2 µm.)

S3. Ar and N_2 isotherms, pore size distributions derived from desorption branches of Ar and N_2 isotherms, and pore size distributions calculated from absorption and desorption branches of Ar isotherms, respectively, of PMFI zeolite before and after TiO_2 ALD

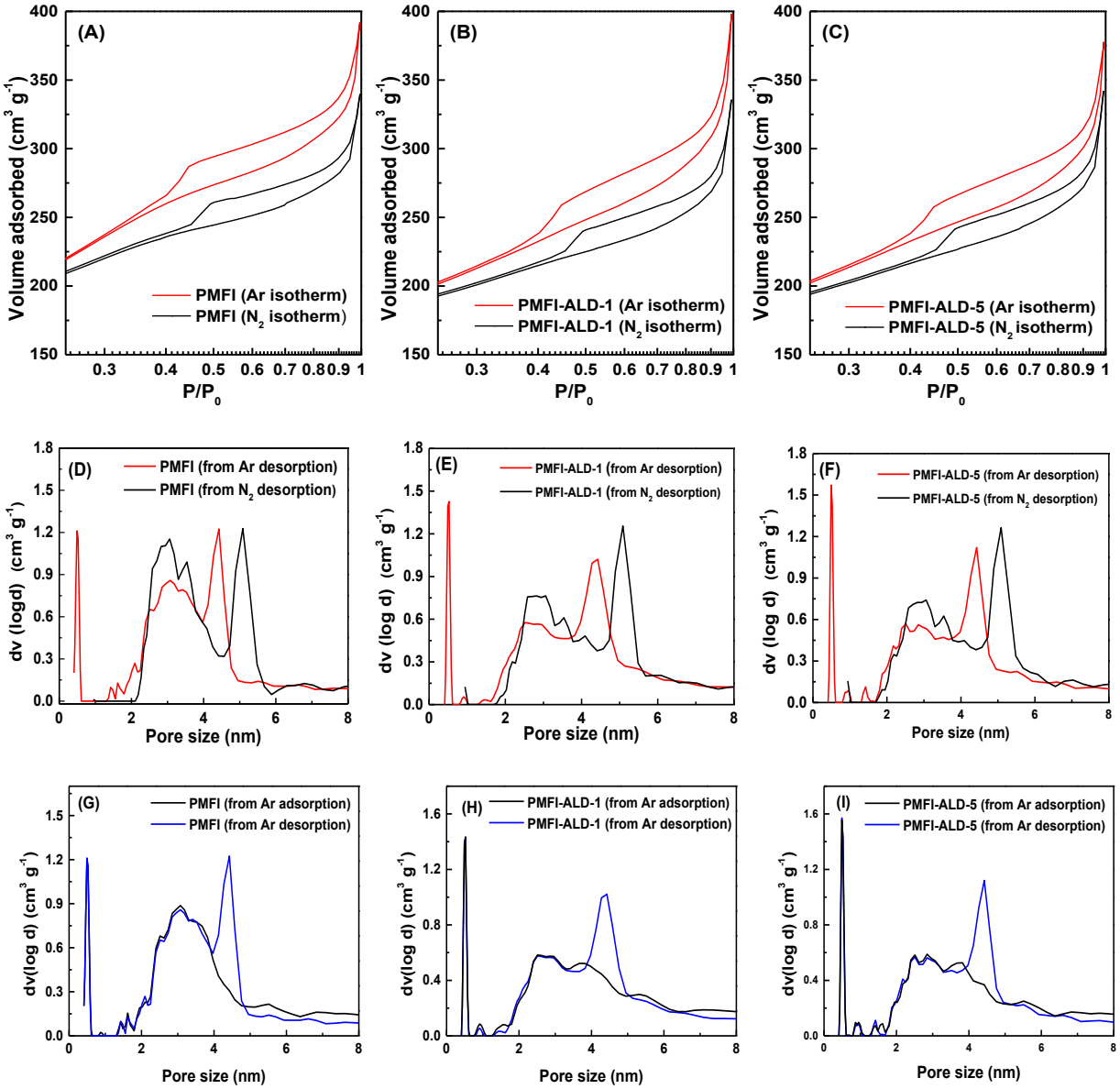

Fig. S2. Ar and N_2 isotherms of PMFI (A), PMFI-ALD-1 (B), and PMFI-ALD-5 (C) zeolites. Their pore size distributions calculated from desorption branches of Ar and N_2 isotherms are shown in (D)-(F) in sequence. For comparison, the pore size distributions from adsorption and desorption branches of Ar isotherms are included in (G)-(I).

S4. Ar and N_2 isotherms, pore size distributions derived from desorption branches of Ar and N_2 isotherms, and pore size distributions calculated from absorption and desorption branches of Ar isotherms, respectively, of PMWW zeolite before and after TiO_2 ALD

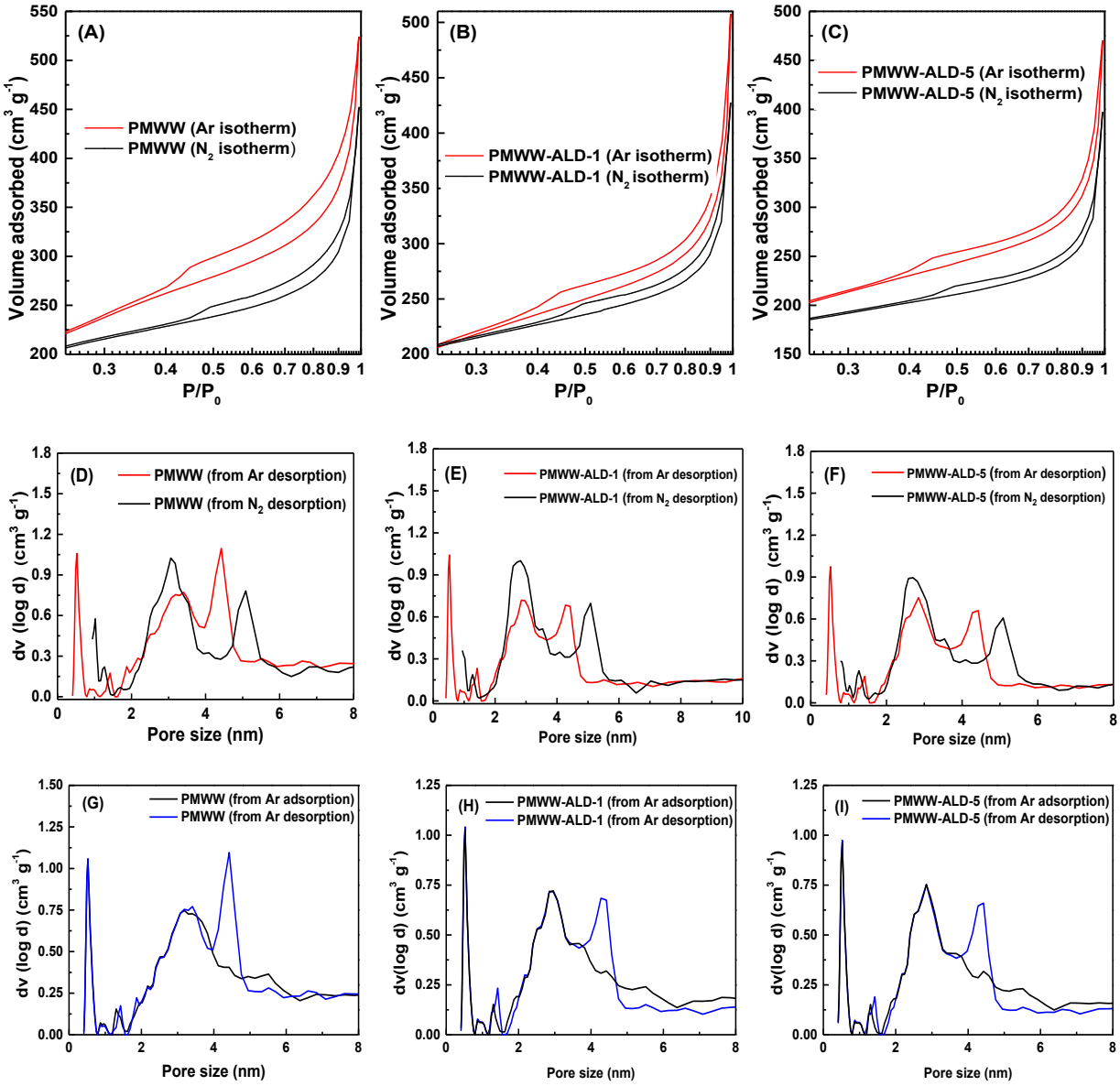

Fig. S3. Ar and N_2 isotherms of PMWW (A), PMWW-ALD-1 (B), and PMWW-ALD-5 (C) zeolites. Their pore size distributions calculated from desorption branches of Ar and N_2 isotherms are shown in (D)-(F) in sequence. For comparison, the pore size distributions from adsorption and desorption branches of Ar isotherms are included in (G)-(I).

S5. Surfactant content in precursors of PMFI and PMWW zeolites

The TGA measurement was done using a thermogravimetric analyzer (TGA-50, Shimadzu) to quantify the contents of organic components in MCM-22(P), swollen MCM-22(P), and multilamellar MFI samples (Fig. S3). Multilamellar is the precursor that was gone through pillaring step to produce PMFI. MCM-22(P) is the precursor to produce swollen MCM-22(P) that was exposed to the pillaring step to produce MCM-36. The results show that multilamellar MFI contains 38.41wt% $C_{22\text{-}6\text{-}6}$ surfactant template, MCM-22(P) has 18.02wt% HMI (hexamethyleneimine), and swollen MCM-22(P) has 34.54wt% organics that is equivalent to 18.02wt% HMI and 16.52wt% CTAB (cetyltrimethylammonium bromide) surfactant used in the swelling process.

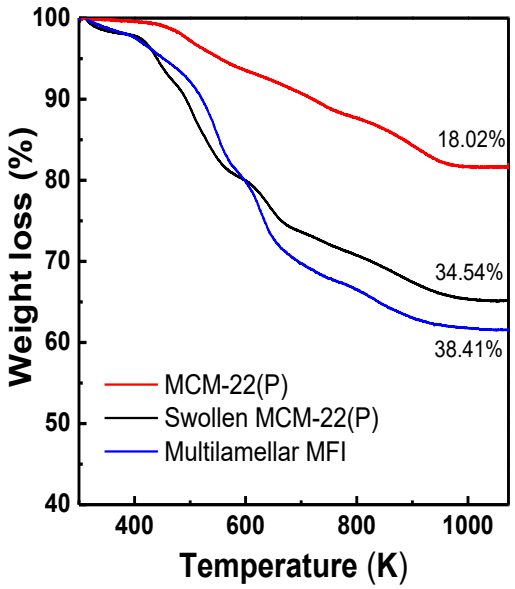

Fig. S4. Organic contents in precursors of PMFI and PMWW zeolites quantified by TGA measurement.

S6. Characterization of PMFI and PMWW zeolite before and after TiO_2 ALD using Scanning Transmission Electron Microscopy with a high annular dark field detector (STEM-HAADF)

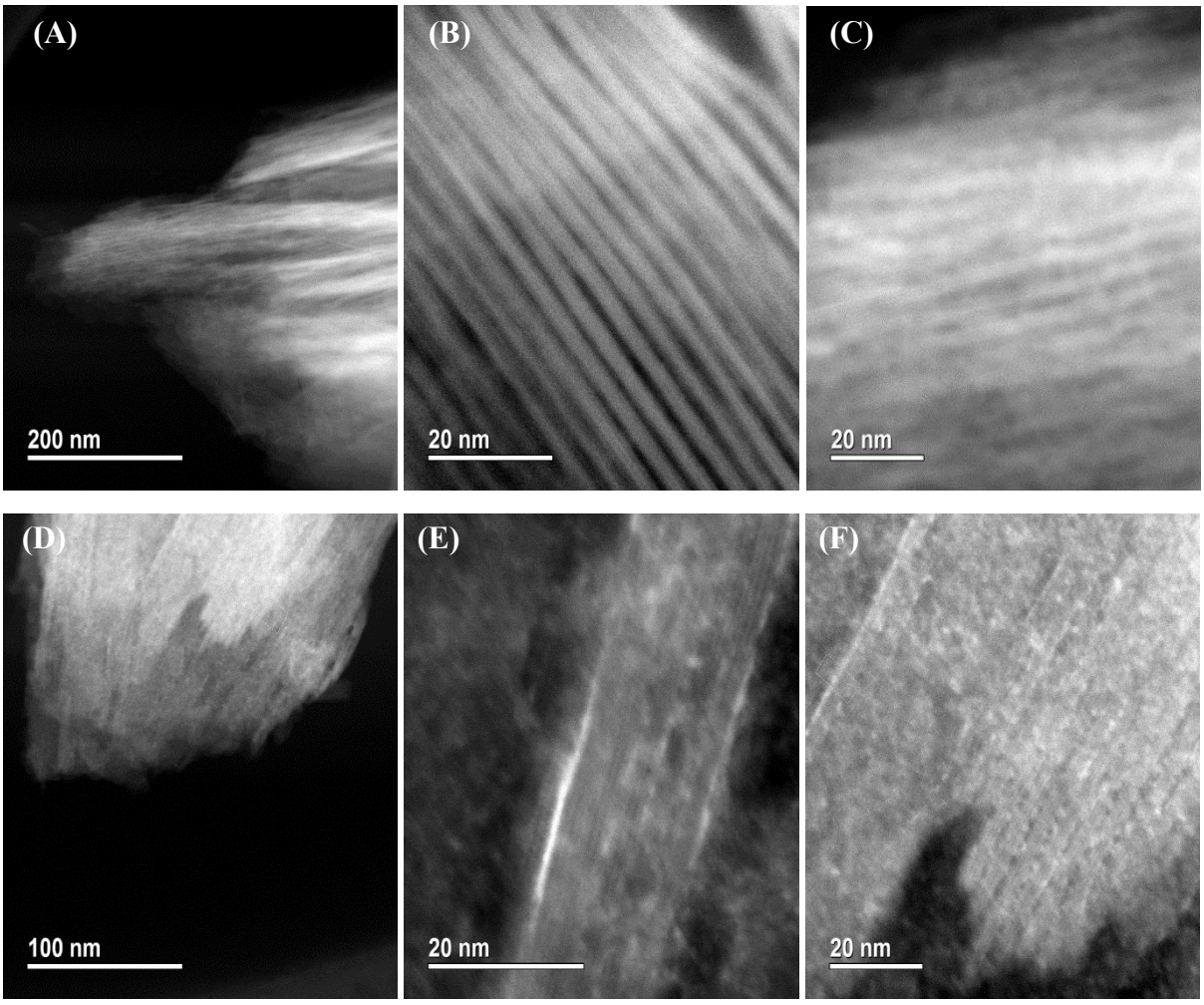

Fig. S5. STEM-HAADF images of PMFI ((A)-(C)) and PMFI-ALD-5 zeolites ((D)-(F)) shown at different magnifications.

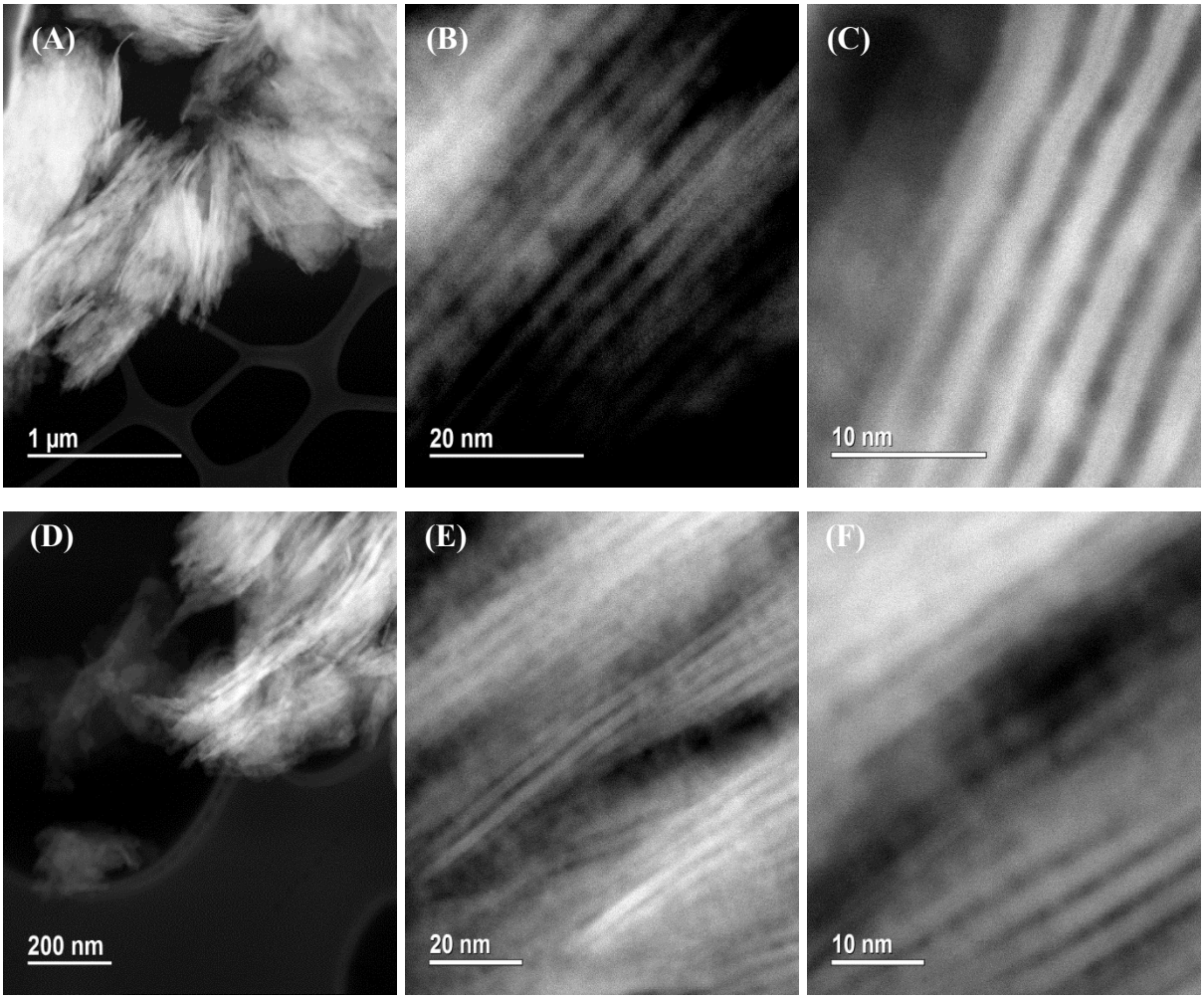

Fig. S6. STEM-HAADF images of PMWW ((A)-(C)) and PMWW-ALD-5 zeolites ((D)-(F)) shown at different magnifications.

References:

[1] M. Choi, K. Na, J. Kim, Y. Sakamoto, O. Terasaki, R. Ryoo, Nature 461 (2009) 246-249.

[2] L. Emdadi, Y. Wu, G. Zhu, C.-C. Chang, W. Fan, T. Pham, Lobo. R. F, D. Liu, Chem. Mater. 26 (2014) 1345-1355.

[3] D. Liu, A. Bhan, M. Tsapatsis, S. Al Hashimi, ACS Catal. 1 (2010) 7-17.

[4] S. Maheshwari, E. Jordan, S. Kumar, F.S. Bates, R.L. Penn, D.F. Shantz, M. Tsapatsis. J. Am. Chem. Soc. 130 (2008) 1507-1516.